Proceedings World Geothermal Congress 2026
Calgary, Canada, June 8 – 11, 2026

Connecting High- And Low-Pressure Geothermal Wells Using a Supersonic Ejector: Analysis of Field Tests at the Theistareykir Geothermal Power Plant

Ximena Guardia Muguruza[1]*, Guðrún Sævarsdóttir[1], Yonatan Afework Tesfahunegn[1], Karl Emil Sveinsson[2], Hilmar Már Einarsson[2], Hugo Ernesto Quinteros Segovia[3], María Sigríður Guðjónsdóttir[1]
Reykjavik University[1]*, Landsvirkjun[2], GRO-GTP[3]
*ximena21@ru.is

Keywords: Supersonic ejector, geothermal wells, underpressure, geothermal fluid extraction.

ABSTRACT

An ejector is a static device that uses a high-pressure fluid to induce fluid flow from a low-pressure source, resulting in a combined flow with an intermediate outlet pressure. In 2021, the power company Landsvirkjun tested a rudimentary subsonic ejector at its Theistareykir Geothermal Power Plant in Iceland to use the high-pressure fluid from well ThG-11 to induce flow from the low-pressure well ThG-15. The tests showed that entrainment from well ThG-15 was achieved. However, well ThG-11 operated at less than half its normal pressure operating conditions, as it was disconnected from the plant during testing. In 2024, we designed and built a supersonic ejector with a convergent-divergent nozzle to evaluate its performance under normal pressure operating conditions of well ThG-11, but at 10% of its usual mass flow. Differential pressure sensors, absolute pressure sensors, temperature gauges, and orifice plates were used to measure pressure, temperature, enthalpy, and mass flow in different setup parts. The results confirmed that the ejector successfully entrained fluid from well ThG-15 when the pressure difference between wells ranged from 9.9 to 26.3 bar, achieving a maximum entrainment ratio of 0.38. This corresponded to a 3.4 bar pressure gain in the secondary flow and an additional exergy rate of 269.2 kW, representing a 9.1% increase in the exergy delivered from well ThG-11. Scaling to full capacity suggests a potential additional exergy rate of 1.96 MW, which translates to approximately 1.37 MWe assuming a 70% exergetic efficiency for the power block.

1 INTRODUCTION

A significant operational challenge in geothermal power is the lack of sufficient fluid pressure from wells to integrate them into the power plants, which occurs in new wells (Sveinbjornsson, 2014) and in existing wells over time (Aydin et al., 2020). This renders them inoperable once their pressure falls below the plant's steam gathering system pressure. Mitigating this problem often requires drilling expensive make-up wells, costing approximately USD 5-7 million per well (Akindipe & Witter, 2025). Globally, about 16% of geothermal wells require re-drilling, and 5.6% rely on mechanical pumping to sustain production (IFC, 2013). In Iceland, approximately 10% of production wells are economically marginal for conventional power generation due to low wellhead pressure (Sveinbjornsson, 2014).

Ejectors offer a potential solution to this challenge. These static devices use a high-pressure motive fluid (e.g., from a high-pressure geothermal well) that expands through a nozzle, creating suction to entrain a lower-pressure secondary fluid (e.g., from a low-pressure geothermal well). The streams are mixed and recompressed in a diffuser to an intermediate pressure (McGovern et al., 2012; Zine et al., 2019; Guðjónsdóttir et al., 2023). By raising the pressure in unproductive wells to the plant's operating threshold, ejectors can extend wells' lifespans, increase power output, and reduce the need for new drilling.

Ejector operation is defined by its nozzle design. Convergent nozzles produce subsonic flow with a moderate pressure drop, while convergent-divergent nozzles accelerate the primary fluid to supersonic velocities at the nozzle outlet due to fluid expansion in the diverging section, enabling a much greater pressure reduction (White, 2016).

Ejectors are conventionally used in geothermal power plants to extract non-condensable gases from condensers (Yamin et al., 2020). However, their application for extracting fluid from low-pressure wells lacks robust experimental validation. A 1999 patent proposed a system but provided no operational details (United States Patent No. 5899273, 1999). Later, a project at the Hellisheiði Power Plant used an ejector to mix fluid streams to mitigate scaling; however, its results were not published (Guðjónsdóttir et al., 2023). This highlights a gap in the experimental support for the use of ejectors for fluid extraction in geothermal wells.

In 2021, a subsonic ejector was tested at the Theistareykir power plant, using high-pressure fluid from well ThG-11 to induce fluid from the low-pressure well ThG-15. The ejector reduced the ThG-11 supply pressure by 20.6%. However, this reduction was only adequate for the test conditions, where the pressure of well ThG-11 (12.6–15.4 bar_g) was much closer to that of well ThG-15 (9.9–11.5 bar_g), as both wells were connected to a separator. If both wells run at full capacity and are connected to the steam gathering system, the pressure in well ThG-11 is higher (25.0–30.0 barg), while that in well ThG-15 is lower (less than 8.5 bar_g), requiring a much greater pressure reduction (Guardia et al., 2023). To address this, a supersonic ejector with a convergent-divergent nozzle was proposed by Guardia et al. (2023). An analytical model demonstrated that this design could elevate the entrained fluid's pressure above the steam-gathering system's pressure (9.5-10.0 barg), potentially generating an additional 0.8 MWe at full capacity of both wells (Andal et al., 2023).

In 2024, a supersonic ejector was designed based on this model and tested at the Theistareykir power plant under normal well pressures of wells ThG-11 and ThG-15, but for around a tenth of the mass flow capacity of both wells. This study analyses the data collected from those tests.

2 MATERIALS AND METHODS

2.1 Ejector design and manufacturing

2.1.1 Ejector design

The designed supersonic ejector comprised two key components: a convergent-divergent nozzle and a mixing chamber. The mixing chamber consisted of four sequential sections: a suction chamber, a constant-pressure mixing section, a constant-area mixing section (CAMS), and a diffuser. Figure 1 provides a schematic of the defined state points used to obtain the ejector's internal diameters using the analytical model developed by Andal (2023). These points are: primary fluid entrance (1), nozzle throat (2), nozzle exit (3), primary fluid at the hypothetical throat, which is where the secondary flow is assumed to have reached sonic velocity (Huang & Chang, 1999) (4), secondary fluid entrance (5), secondary fluid at the hypothetical throat (6), CAMS inlet (7), CAMS exit (8), and diffuser exit (9). A critical design parameter, the Nozzle Exit Position (NXP), is the distance from the nozzle exit (point 3) to the start of the suction chamber's convergent section (Yan et al., 2012).

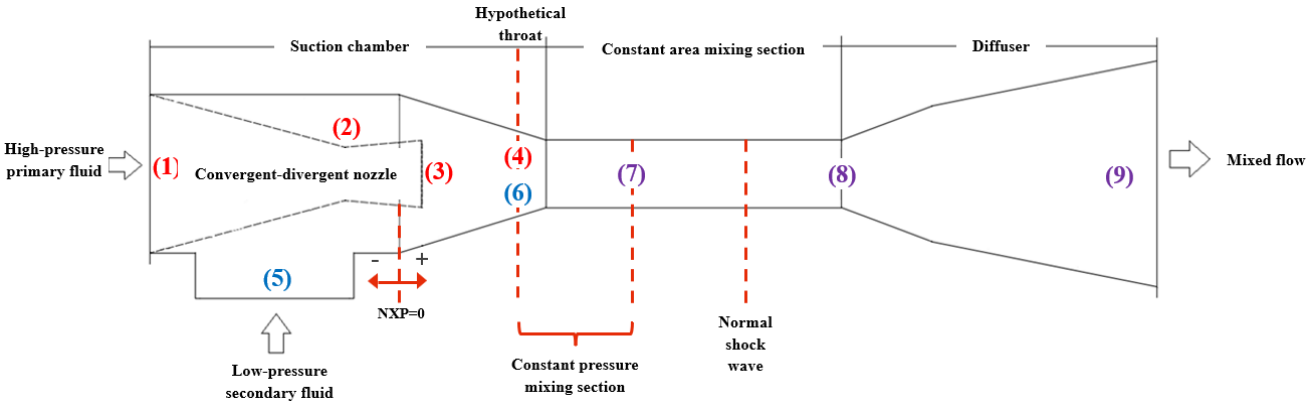


Figure 1. Schematic of the supersonic ejector and flow positions used for the analytical model calculations (from Andal, 2023). Schematic adapted from Ding et al. (2016).

The calculations considered a primary flow entering at 30.0 bar_g pressure and 2.9 kg/s mass flow coming from the primary well ThG-11, a secondary flow from the secondary well ThG-15 entering at 8.0 bar_g pressure and 1.7 kg/s mass flow and an outlet pressure of 9.8 bar_g.

2.2 Field tests

2.2.1 Equipment and setup

The supersonic ejector was installed between the pipelines of wells ThG-11 and ThG-15 using weld neck flanges. The primary fluid mass flow rate and pressure from well ThG-11 were measured 10.5 m upstream of the ejector inlet. At this location, an orifice plate was installed alongside static pressure sensors ($P1_1$, $P1_2$) and a differential pressure sensor ($dP1_3$). Similarly, the mixed flow parameters were measured 2.5 m downstream of the ejector outlet. This setup included an orifice plate, static pressure sensors ($P3_2$, $P3_3$ and $P3_4$), and a series of differential pressure sensors ($dP3_1$, $dP3_2$, $dP3_3$ and $dP3_4$). Additional static pressure sensors were mounted directly on the ejector body: three in the mixing chamber and constant-area mixing section ($Ejector_{P1}$, $Ejector_{P2}$, and $Ejector_{P3}$), and one at the ejector outlet ($P3_1$). Temperature sensors were positioned near well ThG-11 ($T1$), well

ThG-15 ($T2$), and downstream of the ejector's outlet ($T3$). Figure 2 illustrates the experimental setup, including the locations of the orifice plates and sensors, while Figure 3 provides photographs of the installed equipment.

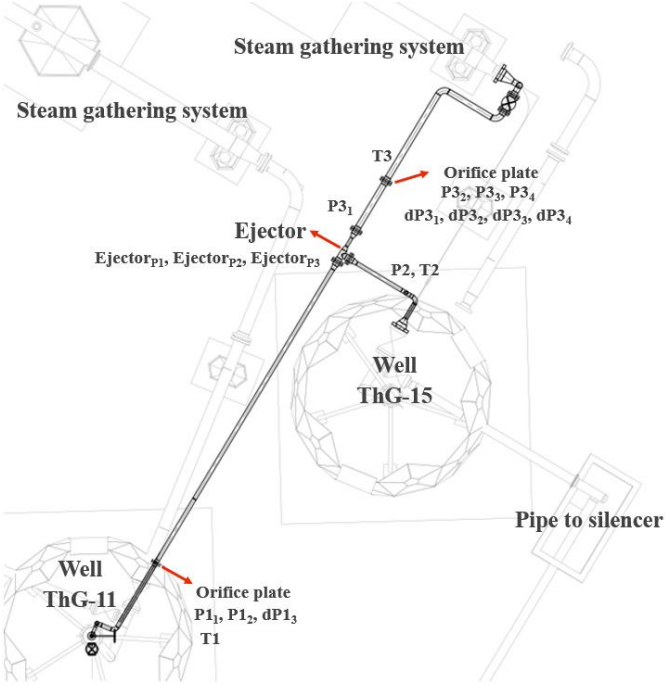


Figure 2. Schematic of the setup and the relevant pressure and temperature sensors.

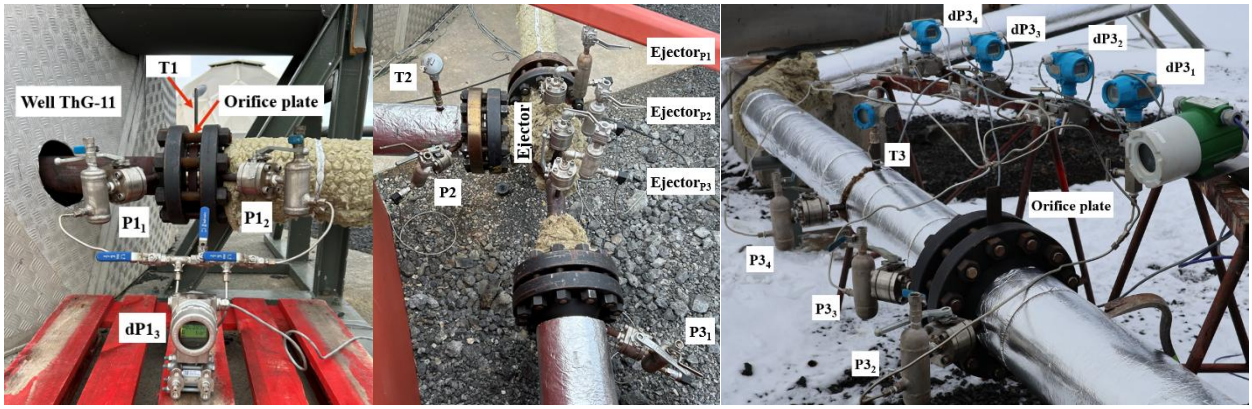


Figure 3. Mounted equipment and sensors upstream of the ejector (left), in the ejector area (middle) and downstream of the ejector (right).

2.2.2 Testing process

The test had 2 main testing periods (see the timeline in Figure 4):

- Testing period 1 (09:41:00–11:51:55 hours, up to the first light blue dashed vertical line in Figure 4): The pressure at well ThG-15 was held constant at an average of 8.1 bar_g, while the pressure at well ThG-11 was gradually reduced from 28.5 to 8.5 bar_g by closing the valve controlling the primary fluid flow to the ejector.
- Testing period 2 (12:56:55–14:05:55, starting from the second light blue dashed vertical line in Figure 4): The primary fluid valve was fully opened to get the maximum pressure of 28.5 bar_g again. Subsequently, the secondary fluid valve was gradually opened to stabilise flow conditions.

Figure 4 shows the complete dataset of measured values, including pressures of the primary and secondary fluids and their corresponding entrained mass flow rates, which were determined using the three-point differential pressure method with orifice plates.

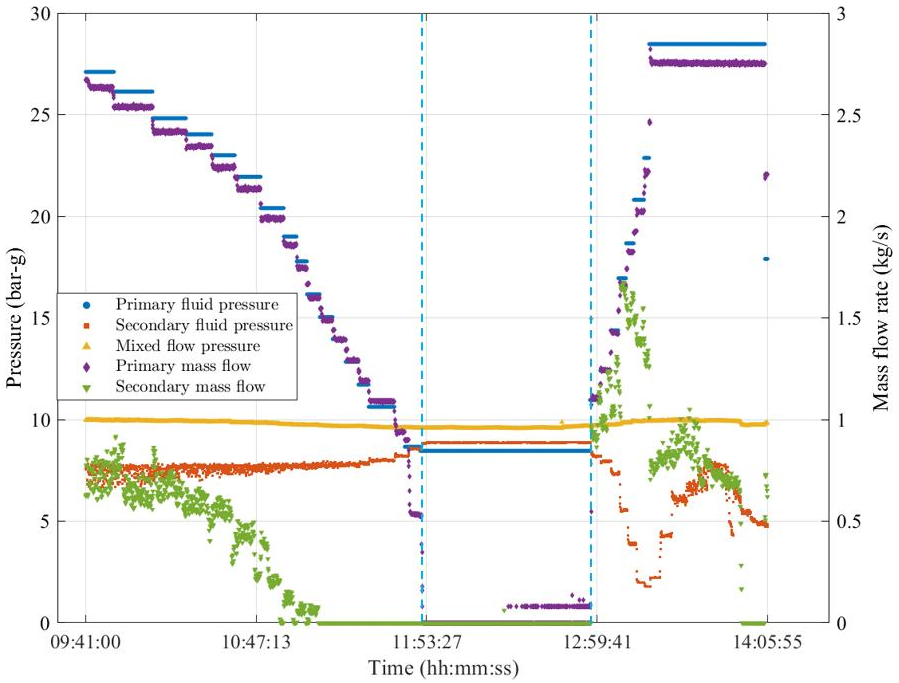


Figure 4. Pressure and mass flow rates obtained from the test. The light blue lines represent the limit of testing periods 1 and 2.

3 RESULTS AND DISCUSSION

3.1 Analysis of measured data

As shown in Figure 4, for testing period 1, the secondary fluid entrainment varies directly with the primary fluid pressure; any decrease in primary fluid pressure results in a proportional reduction in secondary mass flow entrainment, until no mass flow is entrained. During testing period 2, this relationship became less apparent as the secondary fluid pressure was actively adjusted to maintain stable conditions. Thermodynamically inconsistent data from the initial phase of testing period 2 were discarded for the analysis.

Figure 5 and Figure 6 present the main results of the whole data set, in terms of the primary fluid pressure (P_1) at the inlet of the ejector (Point 1 in Figure 1), Gained pressure (GP), and Entrainment Ratio (ER) for the testing conditions. The GP refers to the difference between the mixed flow pressure (P_9) at the outlet of the ejector (Point 9 in Figure 1) and the secondary fluid pressure (P_5) at the secondary fluid inlet (Point 5 in Figure 1) (see Equation 1). The ER is the relation between secondary mass flow ($\dot{m}_5$) at the secondary fluid inlet (Point 5 in Figure 1) and primary mass flow ($\dot{m}_1$) at the primary fluid inlet (Point 1 in Figure 1) (see Equation 2).

$$GP = P_9 - P_5 \quad (1)$$

$$ER = \frac{\dot{m}_5}{\dot{m}_1} \quad (2)$$

Test results demonstrate the ejector's performance across a range of conditions. As shown in Figure 5, entrainment of the secondary fluid began once the primary pressure exceeded 17.9 bar_g. The ER increased with primary fluid pressure, reaching a maximum of 0.38. This behaviour aligns with established ejector theory: operation begins in a subcritical mode where ER rises rapidly, reaches a critical point at maximum ER, and then transitions to a critical mode where further pressure increases have little effect on ER (Tang et al., 2021).

For ER values above 0.01, the ejector consistently generated a pressure gain, elevating the mixed flow pressure from 1.8 to 7.8 bar above the secondary fluid pressure (see Figure 6). The maximum observed ER for both testing periods was 0.38, achieved at primary, secondary, and outlet pressures of 28.5 bar_g, 6.6 bar_g, and 9.9 bar_g, respectively. This 3.4 bar pressure gain raised the secondary fluid to the plant's steam gathering system pressure.

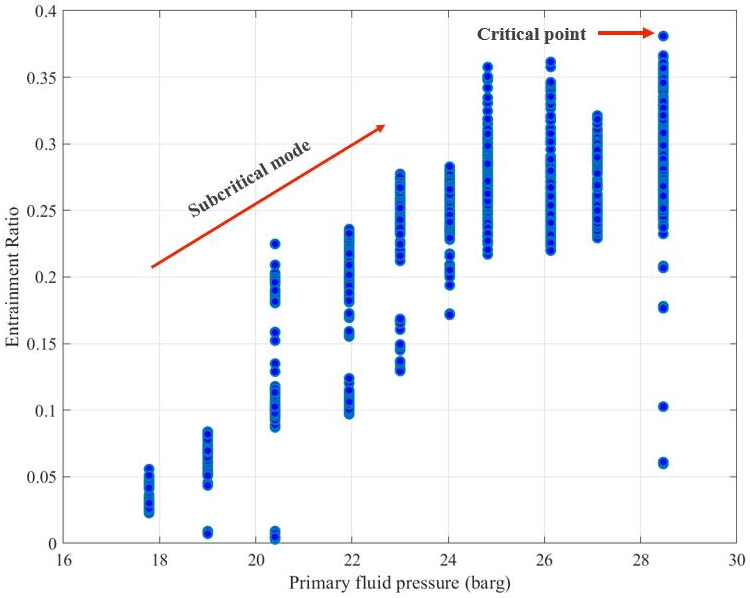


Figure 5. Entrainment ratio vs. primary fluid pressure for testing periods 1 and 2.

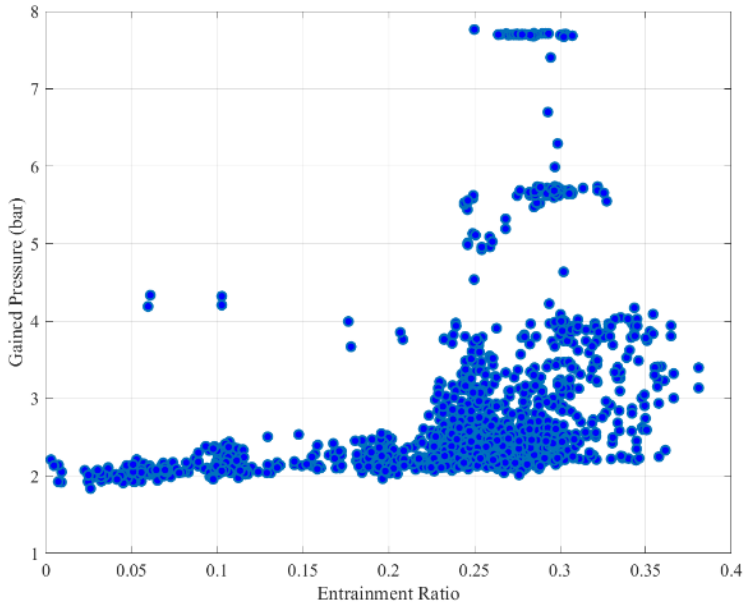


Figure 6. Entrainment ratio vs. gained pressure for testing periods 1 and 2.

3.2 Exergy analysis

Exergy represents the maximum useful work that can be extracted from a system until it reaches equilibrium with its environment (Cengel et al., 2019). It can also be seen as a measure of energy quality that accounts for environmental conditions (Kotas, 2012). The specific exergy e_i of a system is generally composed of four components: Kinetic exergy (e_{KE}), potential exergy (e_{PE}), physical exergy (e_{PH}), and chemical exergy (e_0) (Cengel et al., 2019). Neglecting the potential exergy (e_{PE}) and chemical exergy (e_0), and using appropriate simplifications for kinetic and physical exergy, the specific exergy (e_i) of the ejector fluid becomes:

$$e_i = (h_i - h_0) - T_0(s_i - s_0) + \frac{{v_i}^2}{2} \quad (3)$$

Here, h_i, s_i, and v_i are the specific enthalpy, specific entropy and velocity of the fluid. In contrast, h_0, T_0, s_0 are the specific enthalpy, temperature, and specific entropy of the fluid, respectively, at the environmental state or the dead state, i.e., when the system is in thermodynamic equilibrium with the environment. For this analysis, it was considered that the environmental state was at an average pressure of 1.0 bar_a and a temperature of 2 °C, the temperature registered on November 12th, 2024, in the test area. The exergy transfer or exergy rate by mass

($\dot{E}_i$) can be expressed as the multiplication of the mass flow of the fluid ($\dot{m}_i$) and the specific exergy (e_i) (Cengel et al., 2019):

$$\dot{E}_i = \dot{m}_i \cdot e_i \quad (4)$$

Two other terms were employed for the exergy analysis of the test results: the additional exergy rate and the exergy ratio. Additional exergy rate (ΔE) was calculated as the difference between the exergy rate of the mixed flow at the outlet of the ejector ($E_{mix,out}$) and the exergy rate of the primary fluid at the entrance of the ejector ($E_{primary,in}$):

$$\Delta E = E_{mix,out} - E_{primary,in} \quad (5)$$

The additional exergy rate is calculated solely from the primary fluid's exergy rate. This represents the exergy rate that would directly supply the steam gathering system if the ejector was not present, as the secondary fluid from well ThG-15 cannot be entrained under normal operating conditions. On the other hand, the exergy ratio (R_E) can be derived from the additional exergy rate (ΔE) equation as follows:

$$R_E = \frac{E_{mix,out} - E_{primary,in}}{E_{primary,in}} \quad (6)$$

Figure 7 presents the additional exergy rate (ΔE) achieved through ejector implementation as a function of the time-series data for the primary and secondary mass flow rates.

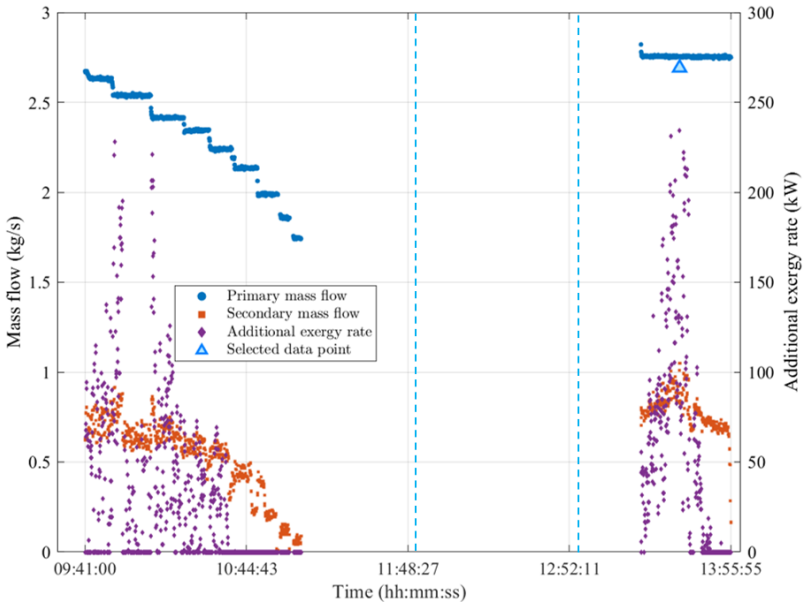


Figure 7. Additional exergy rate for time-series data of mass flow rate during testing periods 1 and 2. The light blue lines represent the limit of testing periods 1 and 2.

As shown in Figure 7, during testing period 1, the primary mass flow decreased due to a reduction in the primary fluid pressure. While the secondary mass flow decreased, an additional exergy rate was still obtained whenever the secondary flow was entrained, with a minimum of 0.5 kg/s. During testing period 2, an additional exergy rate was again observed during secondary flow entrainment, with peak values occurring when the primary and secondary flows were maximum. The test achieved these conditions at 13:35:40 hours (see light blue triangle in Figure 7), where the primary fluid pressure reached 28.5 bar_g with a mass flow of 2.76 kg/s, and the secondary fluid pressure was 6.6 bar_g with a mass flow of 1.05 kg/s. Under these parameters, the ejector achieved an entrainment ratio (ER) of 0.38 and an additional exergy rate of 269.2 kW, as indicated by the light blue triangle in Figure 7.

Figure 8 shows the entrainment ratio (ER) versus the exergy ratio (R_E).

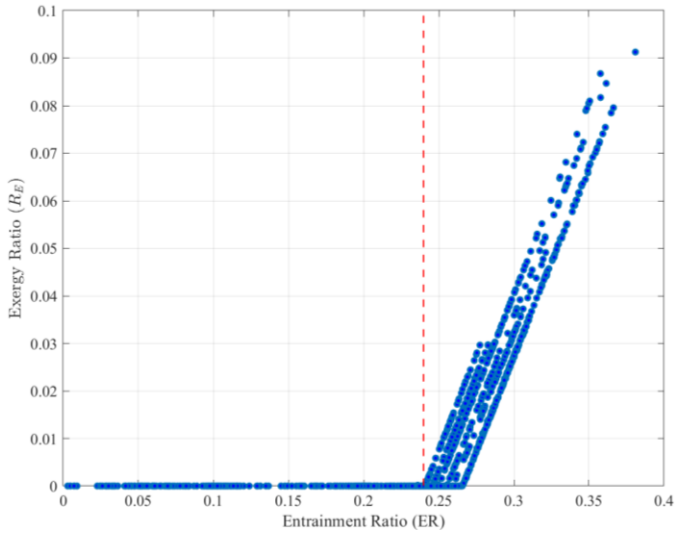


Figure 8. Entrainment ratio vs. exergy ratio for testing periods 1 and 2.

As shown in Figure 8, the ejector exhibits two distinct operating regimes based on the ER. For ER values below 0.24, the R_E is zero, which means that the exergy rate of the mixed flow at the outlet of the ejector ($E_{mix,out}$) and the exergy rate of the primary fluid at the entrance of the ejector ($E_{primary,in}$) are equal. In this regime, the high-velocity primary flow interacts with the minimal secondary flow, creating significant turbulent shear losses and exergy destruction during mixing. Slight increases in ER increase exergy losses, as the exergy of the entrained secondary flow does not compensate for the irreversibilities of mixing. With ER above 0.24, the system transitions to a more efficient regime and the R_E starts to be positive. Here, the secondary flow becomes sufficient to absorb the primary flow's kinetic energy, reducing the shock wave's intensity and the associated exergy destruction. Therefore, an ER of 0.24 represents the critical entrainment ratio that makes the R_E positive. Here, the ejector approaches its design point, achieving peak efficiency. Figure 9 shows the Grassmann diagram of the exergy rate calculated for the point of highest ER (light blue triangle in Figure 7).

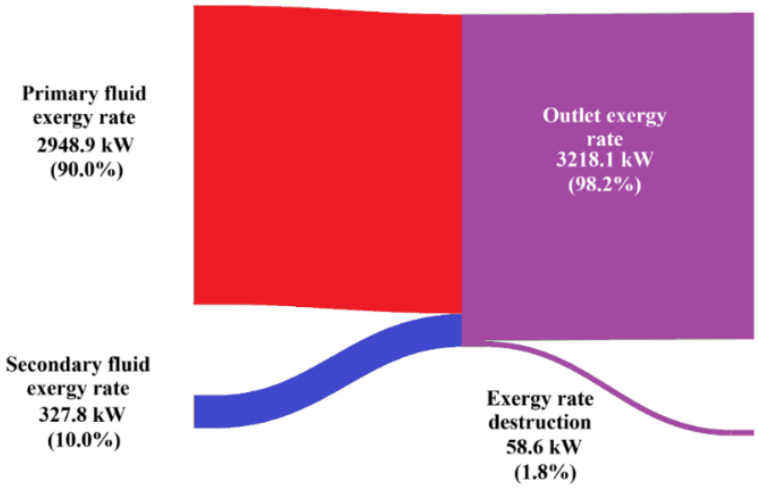


Figure 9. Grassmann diagram of exergy rate for the selected data point shown in Figure 7.

As shown in Figure 9, the primary fluid exergy rate is 2948.9 kW, while the secondary fluid exergy rate is 327.8 kW for the selected data point in Figure 7. The mixed flow at the ejector outlet has an exergy rate of 3218.1 kW, resulting in an exergy rate destruction of 58.6 kW. This destruction arises from several mechanisms. First, the exergy rate is destroyed in the convergent-divergent nozzle (points 1 to 3 in Figure 1) due to entropy generation from internal friction between the steam and the nozzle walls. Second, exergy rate destruction occurs when the primary and secondary fluids start to mix (from point 6 to point 7 in Figure 1), as the high-velocity primary jet collides with the low-velocity secondary fluid. During this process, the primary fluid continues to expand, generating significant turbulence and energy losses (Croquer et al., 2016). Further exergy rate destruction occurs in the CAMS (from point 7 to point 8 in Figure 1), where the shock wave train drastically decelerates the flow in a short length (Croquer et al., 2016), increasing the pressure and enthalpy of the flow. Finally, the diffuser section

(point 9 in Figure 1) contributes marginally to the exergy rate destruction, as the flow velocity reduces and increases the compression effect, having viscous dissipation along the walls (Croquer et al., 2016).

Despite exergy destruction within the ejector, the system achieved a net gain of 269.2 kW for the selected data point, representing a 9.13% increase compared to the exergy of the primary fluid alone. By extrapolating the analytical model developed by Andal (2023) to the full operational capacity of well ThG-11 (28.5 bar_g pressure and 30 kg/s primary mass flow) and for the average pressure of well ThG-15 (8.1 bar_g), the ejector is projected to generate 1.96 MW of additional exergy rate at a 0.38 entrainment ratio. This value translates to approximately 1.37 MWe additional power for the plant, assuming a 70% exergetic efficiency for the power block.

3.3 Pressure, velocity and enthalpy behaviour of the ejector

To analyse the ejector's behaviour, the analytical model developed by Andal (2023) was applied. The as-built internal diameters of the supersonic ejector were used to compute the pressure, velocity, and enthalpy distributions across different flow positions for the selected data point shown in Figure 7. The model was based on the 1-D analytical frameworks proposed by Huang B. et al. (1999) and Chen et al. (2017), incorporating the primary and secondary fluid pressures and enthalpies at the inlet, and the pressure at the ejector outlet, as key boundary conditions. Figure 10 shows the pressure and velocity profiles obtained from the analytical model.

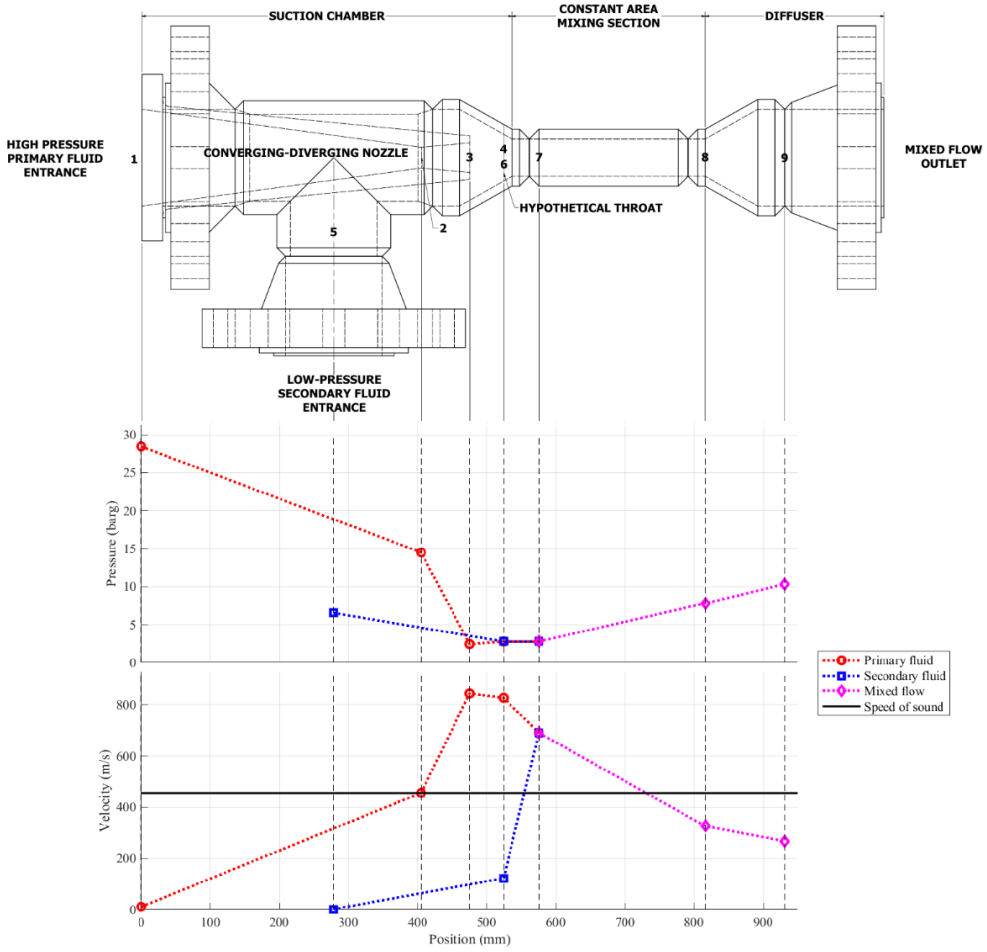
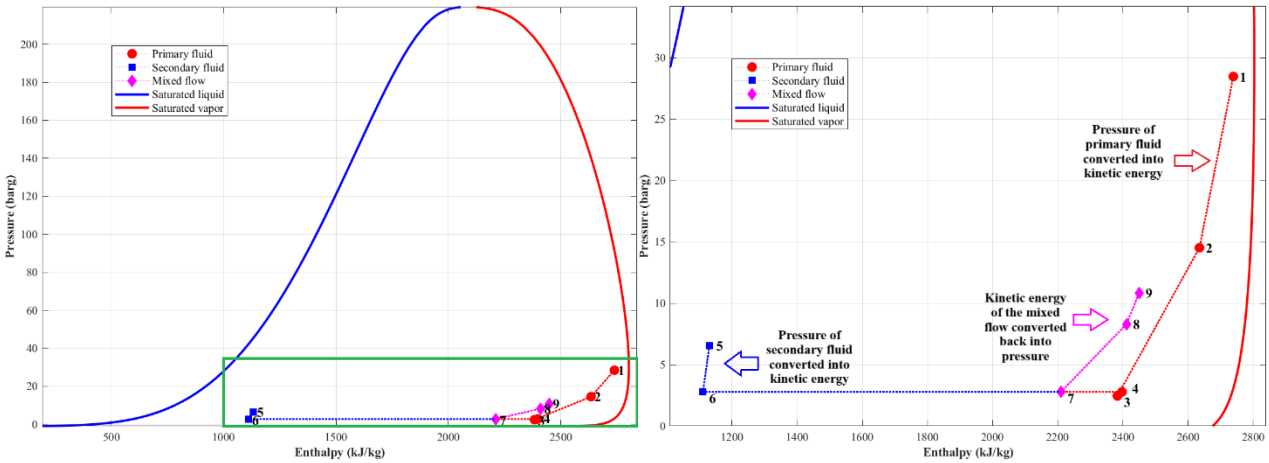


Figure 10. Pressure and velocity profile of primary, secondary and mixed flows for the selected data point shown in Figure 7 according to the analytical model.

The analytical model results in Figure 10 indicate that the primary fluid exits the nozzle (point 3) at a pressure lower than the secondary fluid's inlet pressure (point 5), creating an underpressure that draws the secondary flow in. Both fluids begin mixing at a uniform pressure in the hypothetical throat (points 4 and 6), which is maintained through the CAMS to point 7, as suggested by Huang B. et al. (1999). The pressure then increases inside the CAMS (to point 8). Some authors of 1-D models attribute this pressure rise to a normal shock wave (Huang B. et al., 1999; Chen et al., 2017), while others suggest it results from a compression effect caused by a series of shock waves before the outlet of the CAMS (Zine et al., 2019; Besagni et al., 2016). A final pressure increase occurs in the diffuser (point 9), where the mixed flow exits at an intermediate pressure.

The primary fluid accelerates to sonic velocity at the nozzle throat (point 2) and becomes supersonic at the outlet (point 3), maintaining this velocity into the hypothetical throat (point 4). The secondary fluid also accelerates toward the hypothetical throat (point 6), but it does not reach sonic conditions due to the isentropic efficiency applied in the model. The mixed flow is supersonic until the end of the constant-pressure section (point 7). Its velocity then drops to subsonic after the shock waves (point 8) and decreases further in the diffuser due to the increased area (point 9). To better understand the pressure and enthalpy behaviour within the ejector, Figure 11 presents the Pressure-Enthalpy diagram for the selected data point shown in Figure 7.



a. Complete Pressure-Enthalpy diagram for water. **b. Zoomed region (highlighted in green in part a).**

Figure 11. The pressure-enthalpy diagram for the selected data point, as predicted by the analytical model, is shown in Figure 7. Numbers refer to the location points specified in Figure 10.

Figure 11 shows that the primary fluid's pressure and enthalpy drop through the nozzle (points 1-3), as the pressure is converted into kinetic energy, and keep those conditions up to the hypothetical throat (point 4), while the secondary fluid's pressure decreases from its inlet to the hypothetical throat (points 5-6) also converting the pressure drop into kinetic energy. The fluids mix at uniform pressure up to point 7, increasing the secondary fluid's enthalpy. The mixed flow decelerates through a series of shock waves, converting kinetic energy back into pressure and enthalpy through the CAMS (points 7-8), exiting the diffuser (point 9) at an intermediate state.

4 CONCLUSIONS

The ejector system tested at Theistareykir Geothermal Power Plant successfully provided a maximum additional 269.2 kW of exergy rate, representing a 9.13% increase compared to the exergy rate of the primary fluid alone. Scaling to the full mass flow capacity of wells ThG-11 and ThG-15 suggests a potential additional exergy rate of approximately 1.96 MW for the power plant, which is to approximately 1.37 MWe assuming a 70% exergetic efficiency for the power block. Furthermore, the utilised geothermal fluid serves as a valuable water source for scrubbing processes, underscoring the system's multifaceted relevance for industrial use. The maximum performance was achieved at an entrainment ratio of 0.38, where a high-pressure primary fluid (28.5 bar_g) entrained a lower-pressure secondary fluid (6.6 bar_g), thereby boosting the secondary fluid's pressure to 9.9 bar_g to match the plant's operating pressure.

The system operated effectively across a wide range of primary (8.5–28.5 bar_g) and secondary (1.8–9.1 bar_g) fluid pressures. Its success was enabled by a convergent-divergent nozzle that created supersonic flow and a mixing chamber that ensured fluid combination. While the analytical model proved effective, further CFD and experimental testing are recommended to optimise performance and refine predictive models.

Acknowledgements

This project has received funding from the Rannis Technology Development Fund (Project Number 2112948-0611), the VOR Reykjavik Energy Research Fund, the Rannis Student Innovation Fund, the Reykjavik University Equipment Fund, and the SIF Sustainable Institute and Forum. Their contributions are highly appreciated. We also appreciate the contribution of the managers and operators at Landsvirkjun, especially Hilmar Már Einarsson, Karl E. Sveinsson, Hörður Zoga and Helgi Arnar Alfreðsson, as well as engineers from COWI, Sigurður Jakob Helgason and Kristinn Ingason, who made the structural design of the ejector.

REFERENCES

Akindipe, D., and Witter, E.: 2025 Geothermal Drilling Cost Curves Update, *Proceedings*, 50th Workshop on Geothermal Reservoir Engineering, Stanford University, Stanford, California, United States (2025).

Andal, J.: Master's thesis. Geoejector: Extracting geothermal fluid from a low-pressure geothermal well, Reykjavik University, Reykjavik, Iceland (2023).

Aydin, H., Akin, S., and Senturk, E.: A proxy model for determining reservoir pressure and temperature for geothermal wells, *Journal*, Geothermics, (2020), 101916.

Besagni, G., Mereu, R., and Inzoli, F.: Ejector refrigeration: A comprehensive review, *Journal*, Renewable and Sustainable Energy Reviews, (2016), 373-407.

Cengel, Y., Boles, M., and Kanoglu, M.: Thermodynamics: An engineering approach, McGraw-Hill Education, New York, United States (2019).

Chen, W., Shi, C., Zhang, S., Chen, H., Chong, D., and Yan, J.: Theoretical analysis of ejector refrigeration system performance under overall modes, *Journal*, Applied Energy, (2017), 2074-2084.

Croquer, S., Poncet, S., and Aidoun, Z.: Turbulence modeling of a single-phase R134a supersonic ejector. Part 2: Local flow structure and exergy analysis, *Journal*, International Journal of Refrigeration, (2016), 153-165.

Ding, Z., Wang, L., Zhao, H., Zhang, H., and Wang, C.: Numerical study and design of a two-stage ejector for subzero refrigeration, *Journal*, Applied Thermal Engineering, (2016), 436-448.

Guardia, X., Andal, J., Lárusson, R., Sævarsdóttir, G., Tesfahunegn, Y., Júlíusson, E., Guðjónsdóttir, M.: Connecting high- and low-pressure geothermal wells using an ejector: Analysis of first field tests at the Theistareykir Geothermal Power Plant, *Proceedings*, World Geothermal Congress 2023, Beijing, China, (2023).

Guðjónsdóttir, M., Andal, J., Guardia, X., Lárusson, R., Júlíusson, E., Einarsson, H., Sævarsdóttir, G.: GeoEjector: Extracting geothermal fluid from a low-pressure geothermal well, *Proceedings*, 45th New Zealand Geothermal Workshop, Auckland, New Zealand, (2023).

Huang, B., and Chang, J.: Empirical correlation for ejector design, *Journal*, International Journal of Refrigeration, (1999), 379-388.

Huang, B., Chang, J., Wang, C., and Petrenko, V.: A 1-D analysis of ejector performance, *Journal*, International Journal of Refrigeration, (1999), 354-364.

IFC: Success of Geothermal Wells: A Global Study, International Finance Corporation, World Bank Group, Washington, DC, United States (2013).

Kotas, T.: The exergy method of thermal plant analysis, Paragon Publishing, London, England (2012).

McGovern, R., Prakash Narayan, G., and Lienhard, J.: Analysis of reversible ejectors and definition of an ejector efficiency, *Journal*, International Journal of Thermal Sciences, (2012), 153-166.

Sveinbjornsson, B.: Success of High Temperature Geothermal Wells in Iceland, Iceland Geosurvey, Reykjavik, Iceland (2014).

Tang, Y., Liu, Z., Li, Y., Huang, Z., and Chua, K.: Study on fundamental link between mixing efficiency and entrainment performance of a steam ejector, *Journal*, Energy, (2021), 119128.

White, F.: Fluid Mechanics, McGraw-Hill, New York, United States (2016).

Yamin, W., Makertihartha, I., and Rizkiana, J.: Evaluation on Energy Efficiency Improvement in Geothermal Power Plant with The Application of Load-based Gas Removal System and Cooling Water Pump Control System, *Journal*, Jurnal Rekayasa Proses, (2020), 30–46.

Yan, J., Cai, W., and Li, Y.: Geometry parameters effect for air-cooled ejector cooling systems with R134a refrigerant, *Journal*, Renewable Energy, (2012), 155–163.

Zine, A., Khaled, A., Mehdi, F., and Messaoud, B.: Current Advances in Ejector Modeling, Experimentation and Applications for Refrigeration and Heat Pumps. Part 1: Single-Phase Ejectors, *Journal*, Inventions, (2019), 1–73.